# Temperature stable rare earth magnetic powder Sm-Fe-N based micro magnets with remanence enhanced by easy axis alignment and its application in MEMS actuator

**Huayu Wang[1], Masashi Matsuura[2], Shusuke Yamada[3], Satoshi Sugimoto[4] and Shuji Tanaka[5]**

[1] Department of Robotics, School of Engineering, Tohoku University, Sendai, Japan
[2] Department of Material Science, School of Engineering, Tohoku University, Sendai, Japan

E-mail: huayu.wang@mems.mech.tohoku.ac.jp

Received xxxxxx
Accepted for publication xxxxxx
Published xxxxxx

## Abstract

In this paper, we report an actuator with a magnet made of novel rare earth magnetic powder Sm-Fe-N with diameter of 2 μm to 5 μm. Micro magnets were fabricated by mixing the magnetic powder with wax at temperature of 90ºC. Alignment of the easy axis process was employed to enhance the remanence of the micro magnets. A 8T strong pulse magnetic field was utilized to magnetize the micro magnets. The properties of magnetic powder were revealed with vibrating sample magnetometer (VSM) by measuring micro magnets with various magnetic powder weight loading percentages. In the best condition, the remanence reaches 0.9 T and the energy product reaches 70 kJ/m$^3$. After that, the electromagnetic actuator was fabricated by embedding the magnetic powder in deep-reactive-ion-etched (DRIEed) Si cavity with wax binder and parylene capping. The completed MEMS structure was mounted on a 4-layer printed circuit board (PCB) with embedded coils. Upon the application of a direct current (DC) current for actuation, a displacement of 180 μm was obtained from a device volume of only 1.5 mm$^3$ with a low actuation power consumption of 11.5 mW.

Keywords: rare earth Sm-Fe-N magnetic powder, remanence enhancement, electromagnetic actuator, large displacement, low power consumption

## 1. Introduction

In recent years, the development of microelectromechanical system (MEMS) actuators has drawn an increasing attention in various application scenarios where conventional massive mechanical actuators are unable to be adapted due to the requirement of compactness and low power consumption. During the past decades, a number of MEMS actuators with various characteristics and actuation principles have been developed. Among them, actuators with small size and large displacement are highly desired. To obtain in-plane displacement larger than 100 μm, the actuation principles including electrostatic, thermal, piezoelectric and electromagnetic transduction can be used [1]–[6].

For example, a motion stage based on lever mechanism was reported to achieve almost 100 μm by utilizing electro-thermal actuation [7]. An electrothermal actuator with

 

displacement larger than 200 μm microns was achieved in [8]. However, the thermal actuator needs to be intensively heated up for large displacement, which significantly increases power consumption. Besides, the slow response of thermal actuation is also an awkward drawback. A piezoelectric actuator is usually used for out-of-plane or torsional motion. Several in-plane piezoelectric actuators were reported in [9]–[12], but one with a displacement over 100 μm is based on resonance [9].

In general, an electrostatic comb drive actuator can provide relatively large displacement. For example, a large stroke electrostatic actuator with displacement more than 100 μm was fabricated [13]. A unidirectional displacement of 200 μm was reported [14]. Also, a bi-directional electrostatic actuator with displacement more than 200 μm in each axis was presented [15]. However, such actuators have significantly weak springs, and eventually the force, rigidity and resonance frequency are too small to drive a practical load. In addition, snap-in phenomena, which is lateral pull-in phenomena of comb drive, limits the maximum displacement [16]–[18].

Compared with the actuation principles mentioned above, electromagnetic micro actuators, which utilize Lorentz force generated by the coupling of magnetic field and current, have the advantage of large displacement with relatively low power consumption or low drive voltage and a linear behavior. Therefore, high attention has been paid in developing electromagnetic micro actuators. There are two categories of electromagnetic micro actuators; moving coil type and moving magnet type. The former is widely used for scanning micromirror devices[19]–[27], but it needs a large external magnet. Furthermore, a coil on a MEMS structure is severely heated up by the application of current, because it is suspended by thin spring beams, i.e, thermally isolated. Thus, this paper focuses on the moving magnet type, which may better fit large displacement micro actuators.

Duque *et al*., developed a digital electromagnetic actuator array driven by a coil underneath, the moving magnet and demonstrated displacement more than 1000 μm [28]. Also, the actuation of a moving magnet by achieving displacement of hundreds of microns is also widely used in application of optical image stabilization devices [29]–[33]. Although a large displacement was achieved, they were unable to minimize the size because a conventional bulk magnet was used. On the contrary, Tao *et al*., fabricated an electromagnetic actuator with a size of several milli-meters by manually assembling a micro permanent magnet which was fabricated by bonding Nd-Fe-B powder with resin [34]. However, the displacement is still limited to 10 μm. Han fabricated a bi-directional electromagnetic actuator with displacement of several hundred microns by actuating a moving chessboard magnet [35]. However, the short lifetime and the impossibility of turning it upside down during usage could be problems due to the mechanism character of micro balls and V-groove guideways. The property of a bulk or film magnet plays an important role in the performance of electromagnetic actuators. A strong magnet with high remanence flux is able to generate a large displacement even using a strong support spring or by applying small current. Thus, the selection and fabrication of a micro magnet is one of the most important factors to fabricate a large displacement electromagnetic actuator. The magnet manufactured by the conventional mechanical process has preferable property because of a well-established manufacturing process. However, it is not suitable for MEMS structures because it is not able to provide a sufficient structural accuracy in microscale. An alternative approach is to fabricate a deposition-based magnet with MEMS process. However, the magnetic flux of a magnetic thin film fabricated from electroplating, pulse laser deposition (PLD) or sputtering is extremely small because of a high self-demagnetization field caused by its low aspect ratio [33]–[39]. The application of such kinds of magnetic thin film is impossible for large displacement actuators.

Therefore, to fabricate a micro magnet by bonding magnetic powder within an expected shape of a mold becomes a promising candidate [43]–[47]. However, the related up-to-date research works confronted with a similar problem that Nd-Fe-B powder with micro size is easily oxidized [48]. The magnetic powder is subject to be oxidized and has to be handled in a non-oxygen environment even at room temperature, otherwise the properties of the magnet will be degraded, or even worse the magnetic power burns naturally. Such a property is incompatible with MEMS fabrication process or requires a special fabrication tool. In addition, to increase the remanence, which plays an important role in practical application, is also a challenge for powder-based magnets.

Assuming that a desired micro magnet is available, the integration of the micro magnet with a Si MEMS is not straightforward. The process of assembling the micro magnets with a micro actuator manually is not simple or reproduceable [49]. Considering a monolithic approach, MEMS fabrication process often includes heating steps such as photoresist baking and thin film deposition, which may degrade the magnet. Furthermore, the current fabrication method of an actuation coil is often based on thin film deposition [21], [22], [34]. limiting the number of turns or thickness.

To overcome these challenges, we propose a combination of a strong micro magnet made of antioxidant magnetic powder, a monolithic Si MEMS actuator body with an embedded micro magnet, and a printed circuit board (PCB)-based multilayer coil for displacement greater than 100 μm.

In this paper, we present the micro magnet made of nitride-based rare earth magnetic powder, Sm-Fe-N.

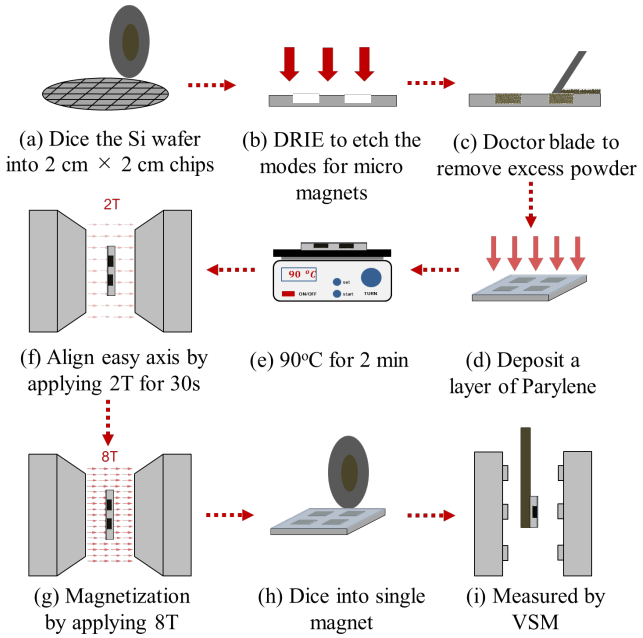


*Figure. 1 Fabrication process of micro magnet. (a) The Si wafer was diced into 2 cm square chips. (b) The Si chip was dry etched to pattern the cavity for micro magnets. (c) The mixture of magnetic powder and wax was loaded into the cavity by doctor blade. (d) A layer of parylene with 3-5 μm thickness was deposited on the whole chip surface. (e) The chip was heated up to 90 °C for 2 minutes to melt the wax. (f) The alignment of easy axis process of magnetic powder was conducted by applying 2 T magnetic field. (g) An 8 T pulse magnetic field was applied to magnetize the micro magnet. (h) The Si chip was diced into single magnet. (i) The single magnet was measured by VSM.*

Compared with Nd-Fe-B powder, Sm-Fe-N powder is stable in air and can be heated up to 110°C, which allows monolithically integration with a MEMS structure. After systematic optimization, we obtained a coercivity, remanence, and energy product of 560 kA/m, 0.9 T, and 70 kJ/m$^3$, respectively. The micro electromagnetic actuators were fabricated by embedding the magnetic powder in a Si-based structure with wax binder and parylene capping. The dimension of the fabricated actuator was as small as 5 mm × 4 mm × 0.5 mm. A 4-layer PCB with a thickness of 0.4 mm was designed for an actuation coil. By the application of a DC current, the performance of actuators with different strength magnets was tested, and a displacement as large as 180 μm was demonstrated.

## 2. Micro Magnet Made of Sm-Fe-N Powder

### *2.1 Fabrication of magnets*

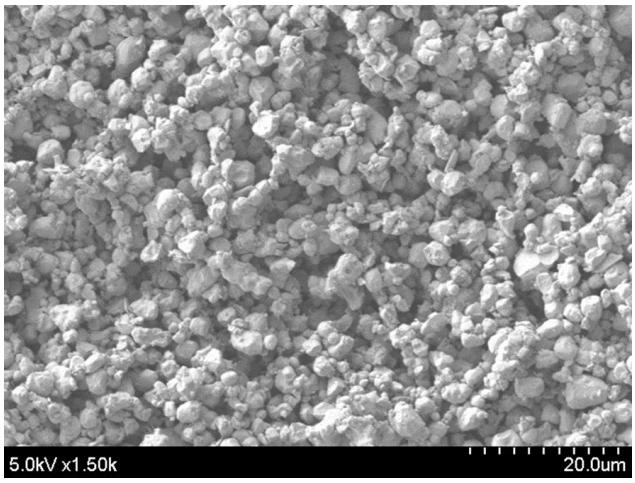


*Figure. 2 SEM image of Sm-Fe-N powder.*

In this study, Sm-Fe-N micro magnets embedded in a Si substrate were fabricated on different conditions according to the process shown in Fig. 1. The fabrication process started with the dicing of a 4-inch Si wafer, and a 2 cm × 2 cm Si chip was then etched by deep reactive ion etching (DRIE) to create the mold for the micro magnet with a lateral dimension of 3 mm × 1 mm and a depth of 0.5 mm. The magnetic powder used here is $Sm_2Fe_{17}N_3$ provided by NICHIA Corporation. As shown in Fig. 2, the diameter of the powder is consistently around 2-5 μm, which allows the powder to form a micro magnet with various dimensions.

Before the fabrication of the magnets, magnetic samples were prepared by mixing different weight percentages of the magnetic powder and wax with a melting point of 75°C in glass tubes. Then the glass tubes were heated to 90°C and stirred by a heater for 2 min. The magnetic powder weight loading percentage of the slurry samples ranged from 80% to 100%. The magnetic slurry was packed into the cavities by doctor blade at a temperature of 90°C. After the mold was cooled down to room temperature, a layer of parylene with a thickness of 3 μm to 5 μm was deposited on the surface to encapsulate the magnetic powder. The Si chip was heated up to 90°C by the heater for 2 min to completely melt the wax. Immediately after that, a 2 T magnetic field was applied to the Si chip for 30 s using an electromagnetic treatment machine (TEM-WV101C-252, TOEI Industry Co. Ltd. Japan) to align the easy axis of the magnetic powder inside the melted wax. The wax was naturally cooled down to room temperature, and froze again to bond the powder. Then, an 8 T pulse magnetic field was applied with a pulsed high field magnetization system (MPM 07, TOEI Industry Co. Ltd., Japan) by increasing the charge voltage from 0 V to 390 V for around 3 min to magnetize the micro magnet at room temperature. Due to all the fabrication processes were all performed in air by manually, high risks to damage the magnet inside the cavity. Besides, when the wax is not

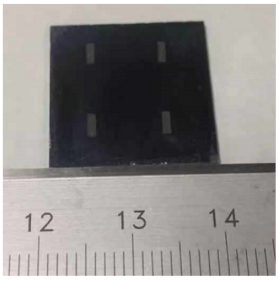


*Figure. 3 Prepared magnet sample. 4 micro magnets are embeded in the 2cm square Si chip. The dimension of one micro magnet is 3 mm × 1 mm × 0.5 mm.*

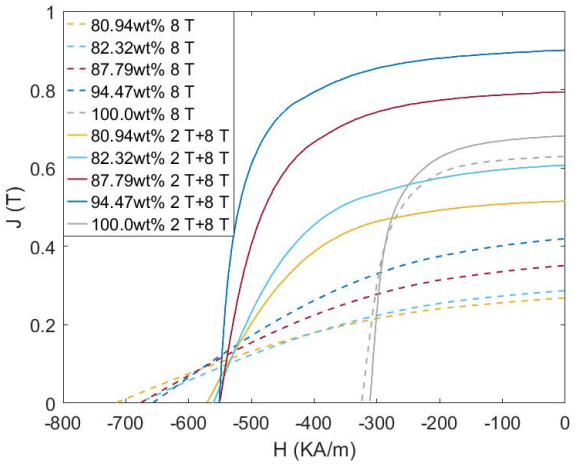


*Figure 4. Comparison of micro magnets with and without performing the alignment of the easy axis process. By the alignment of the easy axis, the remanence of the micro magnets with wax can be increased. The effect of the alignment of the easy axis is not obvious when there is no wax inside the magnet*

*Table 1 Summary of the samples for testing.*

| Sample No. | 1 | 2 | 3 | 4 | 5 | 6 | 7 | 8 | 9 | 10 |
|---|---|---|---|---|---|---|---|---|---|---|
| Dimension | 3 mm × 1 mm × 0.5 mm | | | | | | | | | |
| Magnetic Powder Weght Percentage (wt%) | 80.94 | 82.32 | 86.78 | 94.47 | 100.00 | 80.94 | 82.32 | 86.78 | 94.47 | 100.00 |
| Easy Axis Alignment | 2 T, 2 min, 90 °C | | | | | NA | | | | |
| Pulse Magnetization | 8 T, 300 V, Room Temperature | | | | | | | | | |

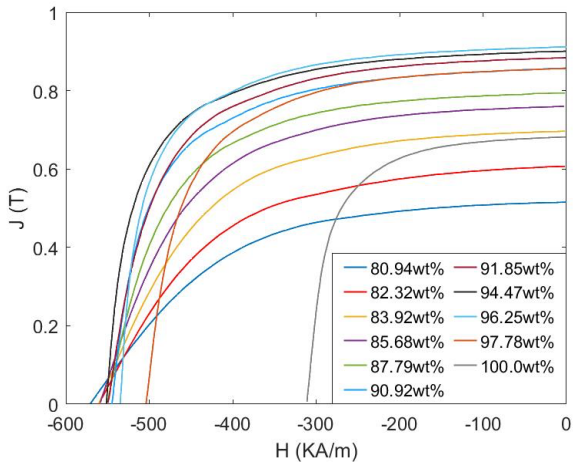


*Figure 5. Demagnetization curve of micro magnets with different powder weight loading percentages. The remanence of micro magnets increases with the increase of powder weight loading percentage. But when the wax is not enough to bond the magnetic powder, the remanence decreases sharply.*

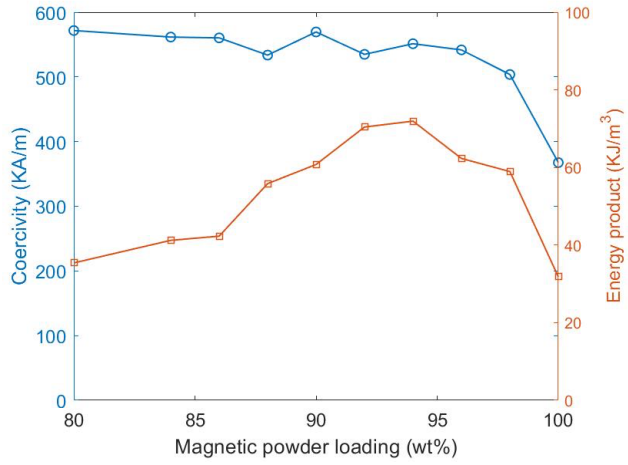


*Figure 6. Coercivity and energy product of micro magnets. When the wax is enough to bond the magnetic powder, the coercivity remains constant and the energy product increases as the increase of magnetic powder weight loading percentage. When the wax is not enough to bond the magnetic powder, both coercivity and energy product decrease sharply.*

sufficient enough to bond the powder, the powder inside the cavity intends to drop out of the cavity. Thanks to the parylene film, the magnetic powder was protected during the following fabrication process after parylene deposition, including heating, easy axis alignment, magnetization, dicing

and measurement. Fig. 3 shows one of the prepared samples. We prepared the magnet samples with and without the

*Table 2 Comparison with previous works.*

| Year | Material | Fabrication | Coercivity (kA/m) | BHmax (kJ/m$^3$) | Magnet Size |
|---|---|---|---|---|---|
| 2020 | CoPt | Electroplate | 1000 | 77 | T100 μm film |
| 2019 | NdFeB/Fe | SU8 bond | 246 | <18 | ø50 μm x T100 μm |
| 2019 | NdFeB | ALD | 700 | <50 | L175 μm x W175 μm x T400 μm |
| 2019 | CoPt | Electroplate | 850 | 56 | T60 μm film |
| 2017 | NdFeB | Resin bond | 772.4 | 18.4 | L600 μm x W600 μm x T200 μm |
| 2016 | NdFeB | ParyleneN/C | 127~1040 | <70 | L4 mm x W4 mm x T400 μm |
| 2016 | CoPt | Electroplate | 800 | 100 | T6 μm film |
| This work | SmFeN | Wax bond | 500~560 | 40~70 | L3 mm x W1 mm x T0.5 mm |

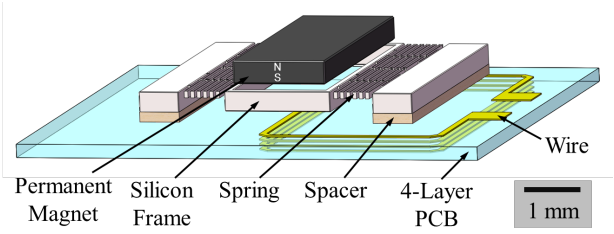


*Figure 7. Schematic of electromagnetic actuator. The actuator mainly consists a permanent magnet, a silicon actuator frame, a 4-layer PCB. The wire in the PCB of each layer is connected by via hole. The magnet is suspended by silicon springs. The actuator is assembled with the PCB by utilizing spacers, which can maintain the gap between magnet and the PCB*

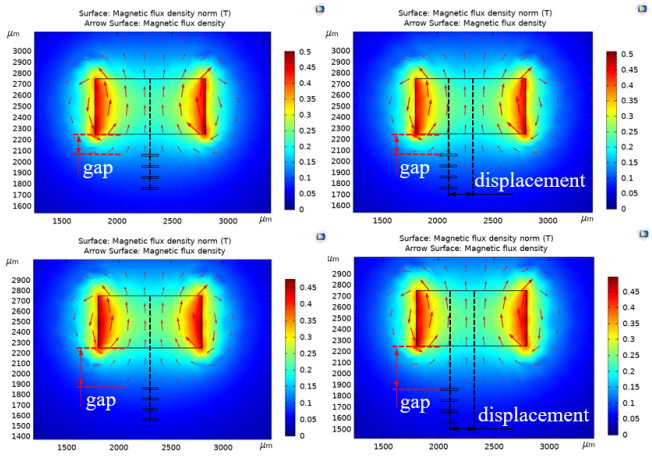


*Figure 8. Magnetic simulation model in COMSOL. The simulation aims to study the Lorentz force generated by the coupling between permanent magnet and current. The 2D model consists of a permanent magnet with magnetic flux in vertical direction and four actuation wires, which is accordance to the designed PCB. In the simulation, the impact to the Lorentz force caused by the gap that between the permanent magnet and the wire and the permanent magnet displacement in horizontal direction are studied*

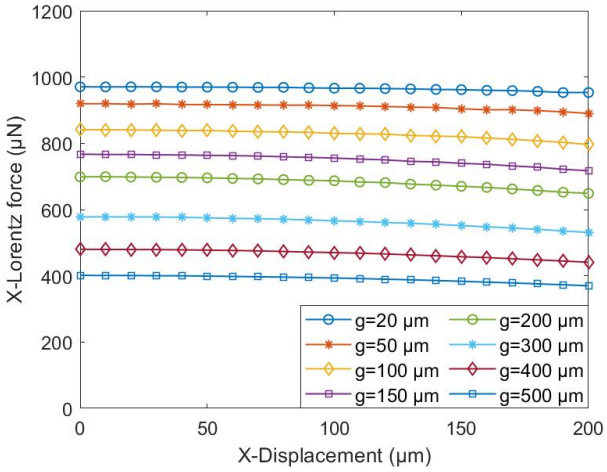


*Figure 9. The Lorentz force in X direction changes neglectable small regardless the position of magnet. With the gap between magnet and PCB decrease, the Lorentz force becomes larger.*

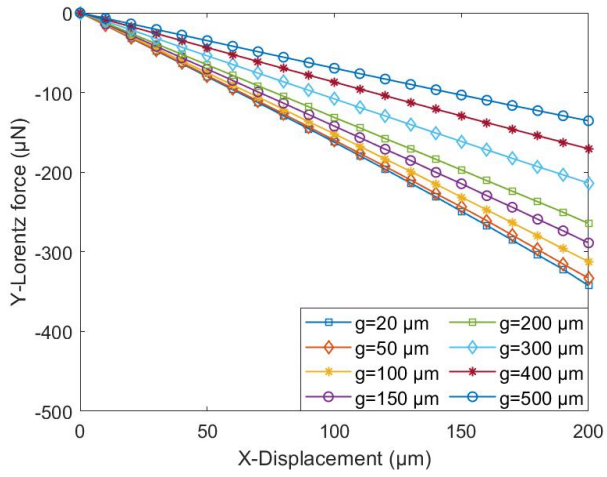

*Figure 10. Lorentz force in Y direction decreases as the increase of gap between magnet and PCB. With the displacement increases, the Lorentz force in Y direction becomes larger.*

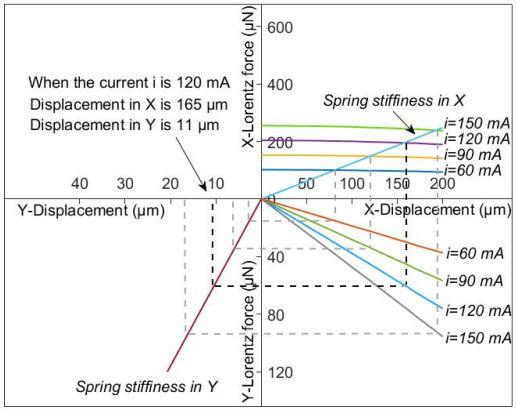


*Figure 11. Prediction diagram for displacements in X and Y directions with different applied currents, I.*

alignment of the easy axis. Table 1 summarizes the conditions of the samples

## *2.2 Measurement method*

The magnet samples were evaluated by a vibrating sample magnetometer (VSM) (BHV-55, Riken Denshi Co. ltd Japan) to find the best magnetic powder loading percentage and to study the effect of the alignment of the easy axis on the characteristics of the magnets. The measurement started with the calibration of the VSM with a Ni reference sample which has the same shape of the magnet sample. After the calibration, the magnet samples were mounted on a rod with vibration frequency of 24 Hz and measured for 5 min per piece. From the VSM, demagnetization curves in M-H format were obtained. To remove the effect of the magnet shape and to know the intrinsic magnetic property, the self-demagnetization field $H_d = -NJ/\mu_0$ , where $N$ is demagnetizing factor, $J$ is magnetization strength, and $\mu_0$ is permeability in vacuum, caused by a magnetic charge on the polar surfaces of the magnet was compensated. $N$ was calculated as 0.59 for this magnet according to [50].

## *2.3 Evaluation results*

Fig. 4 shows the comparison of the magnet characteristics in J-H format with and without the alignment of the easy axis process. The demagnetization curves reveal that the remanence was increased by 60% and the coercivity was decreased by 30% by conducting the alignment of the easy axis. As shown in Fig. 1e, the wax inside the magnet was totally melted when the chip was heated up to 90°C. The powder inside the mixture was able to mechanically rotate when a 2 T magnetic field was applied in Fig. 1f. When the wax froze in Fig. 1f, therefore, the easy axis of the magnetic powder was aligned in one direction. As a result, the

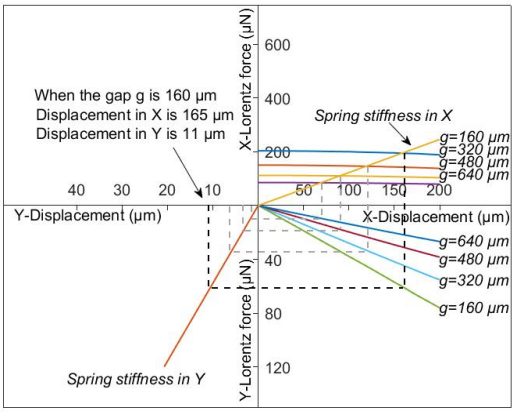


*Figure 12. Prediction diagram for displacements in X and Y directions with different magnet-coil gaps, g.*

remanence flux of the micro magnet was enhanced. However, the effect of alignment of the easy axis was not obvious when there was no wax in the micro magnet. This could be explained that the majority of the powder particles inside the cavity was not able to rotate because of no wax works as binder during the measurement by VSM. As a result, the coercivity and remanence were small.

With adopting the alignment of the easy axis, the magnets with various magnetic powder loading percentages were compared. As found in Fig. 5 and Fig. 6, when the magnetic powder loading weight percentage was below 94%, the coercivity remained around 550 kA/m, the remanence flux increased as the increase of magnetic powder weight loading percentage. However, when the magnetic powder weight loading percentage exceeded 96%, both remanence and coercivity decreased due to a lack of wax to fix the magnetic powder inside the cavity. As a result, the magnetic powder could rotate freely inside the cavity according to the magnetic field by VSM during measurement, which leads to the decrease of coercivity and remanence. When there was no wax inside the cavity, both the remanence and coercivity decreased significantly compared with the best condition.

The energy product as shown in Fig. 6 changes in the same manner as the coercivity. The best weight loading percentage of the magnetic powder is between 90% and 96%. In this case, the remanence could reach as large as 0.9 T and the energy product could reach 70 kJ/m$^3$ as well. The previous works related to the micro magnet are summarized in Table 2. The overall performance of the micro magnets made from Sm-Fe-N could compete with those fabricated

from Nd-Fe-B [21], [25], [36], [39], [44], [47], [51]. Besides, even though the electroplated magnets possess higher coercivity, the real application by utilizing the out of plane magnetic field was not ideal because of the high demagnetization field caused by the shape of thin film. The

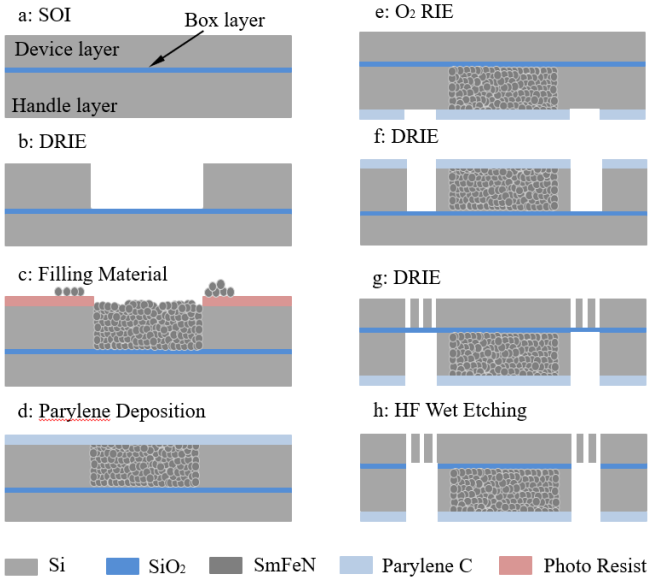


*Figure 13. Fabrication process of magnetic actuator. (a) The fabrication process started with a SOI wafer. (b) The substrate layer was dry etched by deep RIE to pattern the cavity for micro magnet. (c) The mixture of magnetic powder and wax was loaded into the cavity by doctor blade. (d) A layer of parylene with 3 μm to 5 μm thick was deposited on the surface. (e) The unnecessary part of the parylene was removed by $O_2$ plasma. (f) The substrate layer was dry etched to pattern the suspended part of the actuator. (g) The spring was patterned on the device layer. (h) Finally, the structure was released by HF wet etching.*

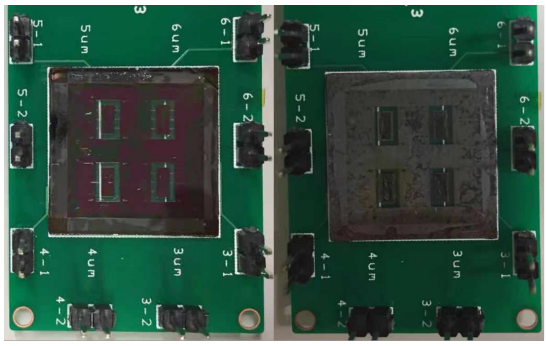

(a) Top side (b) Back side

*Figure 14. Top side and back side of the actuator on the PCB.*

Sm-Fe-N powder could stand with at least 50°C higher temperature than that of Nd-Fe-B with similar diameter [48]. It is found that Sm-Fe-B powder has a promising feature in MEMS application.

## 3. MEMS Actuator Using Sm-Fe-N Micro Magnet

### *3.1 Design*

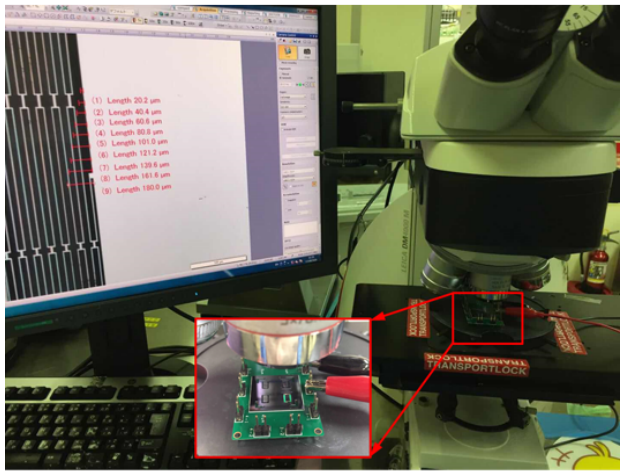

*Figure 15. Experimental setup to evaluate actuator displacement. The displacement of the actuator was measured and recorded by the microscope.*

Fig. 7 shows the schematic of the one axis actuator. A movable magnet made of the Sm-Fe-N powder was embedded in the Si frame suspended by Si springs. The dimension of the actuator was limited within 5 mm × 4 mm × 0.56 mm. A layer of parylene with a thickness of 3 μm to 5 μm was deposited on the surface of the magnet. A PCB with4 layers was designed for an actuation coil as a Cu loop in each layer was connected by via through holes. By taking advantage of the standard manufacture process, the inner diameter of the via through hole is 70 μm and the diameter of the via pad is 140 μm. The actuator was then glued onto the PCB by using spacers to maintain the gap between magnet and PCB.

### *3.2 Finite element method (FEM) simulation*

To evaluate Lorentz force generated by the coupling of the magnetic field and current, FEM simulation was performed utilizing commercial software, COMSOL. In the simulation model, the thickness of the permanent magnet is 0.5 mm and the magnetic flux is defined as 1.3 T in vertical direction. As shown in Fig. 8, both the gap maintained by the spacer and relative position between the magnet and the coil were changed. A DC current of 300 mA was applied in each wire. As shown in Fig. 9, the Lorentz force in X direction is almost constant regardless of the lateral position of the magnet. It becomes larger with the gap *g* decrease. In this simulation,

Lorentz forces of almost 1000 µN and 400 µN were obtained when the gaps were 20 µm and 500 µm, respectively. Multiple coils are helpful to enlarge the Lorentz force compared with single coil. Unfortunately, with the increase of the PCB layers, the distance between the coil in bottom layers with the magnet is also increased. As a result, the contribution from the coils with large distance grows larger

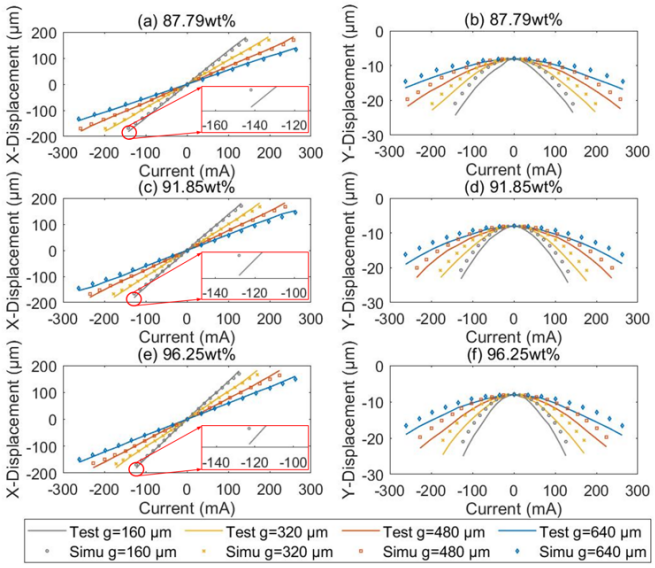


*Figure 16. Displacement vs current. The displacement in both X and Y direction of the actuators with powder weight loading percentage ranged from 87.79wt% to 96.25wt% was measured by microscope*

in Lorentz force in Y direction during the movement which will increase the out-of-plane displacement. Moreover, considering the manufacturing cost, 4-layer PCB is the best candidate for the actuation in our case. In the current design, the simulated spring constant of two Si springs supporting the magnet is 1.24 N/m in X direction, and the displacements of 800 µm and 320 µm are expected at 300 mA.

The Lorentz force in Y direction was also investigated. As shown in Fig. 10, when the X-axis displacement of the magnet is 0 µm, the Lorentz force in Y direction is 0 N. The Lorentz force became larger as the increase of the displacement. Similarly, as the gap became smaller, a larger Lorentz force in Y direction would be generated. Based on FEM simulation, the Y-axis spring constant of the support springs is 5.8 N/m, if the spring width is 6 µm. In order to predict the displacement of the actuator in both X and Y direction, the magnet is defined as the magnetic flux of 0.88 T in simulation which is same with the test result of 91.85wt% magnet. Two scenarios are considered as shown in Fig. 11 and Fig. 12. In Fig. 11, when the gap *g* is defined as 160 µm, the displacements in X and Y directions are predicted as the applied current increased from 30 mA to 150 mA. Similarly, in Fig. 12, when the applied current is defined as 120 mA, the displacement in X and Y directions are predicted with the gap *g* increased from 160 µm to 640µm. Combine the results in Fig. 11 and Fig. 12, when the gap *g* and applied current are 0 µm and 120 mA, the displacement in X and Y are 165 µ and 11 µm, respectively.

### *3.3 Fabrication*

Fig. 13 shows the overall fabrication process flow, which mainly incorporates Si dry etching process and the micro magnet fabrication process. We used a silicon-on-insulator (SOI) wafer, where thickness of, a device layer, a BOX layer and a handle layer were 60 µm, 1 µm and 500 µm, respectively. The handle layer was etched to pattern the cavity of the micro magnet. After that, the cavity was filled with the Sm-Fe-N slurry by doctor blade. Since this was a manual process, it was inevitable for the slurry to distribute on the surrounding surface of the sample. The residual slurry could be removed by stripping away the photoresist. The next step was to deposit a parylene layer with a thickness of 3 µm to 5 µm on the surface. The excess parylene was etched by $O_2$ RIE. Then, the handle layer was etched to pattern the suspended moving plate, followed by the magnetization. The condition is the same with samples in Table 1. The spring was patterned in the device layer by DRIE. Finally, the actuator was released by buffered hydrofluoric acid (BHF) wet etching.

The completed Si actuator is shown in Fig. 14. It was assembled with the PCB and the gap between the PCB and the magnet was maintained by the spacer made by a double side tape. The thickness of spacer could be controlled by adding or removing one layer of tape for 160 µm variance. Then, the spacers with different thickness were prepared for testing the performance of the actuator.

### *3.4 Characterization*

The displacement of the actuators was measured with a microscope as shown in Fig. 15. We varied the magnetic powder weight loading percentage and the gap between the suspending magnet and the PCB to investigate the displacement. The current was supplied with a power source with the maximum current of 262 mA. As shown in Fig. 16, the displacements in both X and Y directions increased as the increasing of actuation current, and the largest displacement in X direction and Y direction were 180 µm and 17 µm, respectively. As the magnetic powder weight loading percentage of the magnetic powder increased, the displacement increases with the same current. Large Lorentz force occurred by the coupling between the magnet with large remanence and magnetic field induced by the PCB circuit. The coupling depends on the gap as shown in the simulation result, becomes weak with large thickness of the spacer. As shown in Fig. 16c and e, the actuator with the

magnet of 91.25wt% and 96.25wt% showed the smallest actuation current of around 120 mA to achieve the largest displacement of 180 μm when the gap between the magnet and the PCB was 160 μm in X direction.

Meanwhile, compared with the simulation results, the measured displacement is identical with the simulated value which could be observed in Fig. 16. The variances in X and Y direction when achieving the largest displacement is within 15 μm and 3 μm, respectively, which proves that the predictions in Fig. 11 and Fig. 12 are reasonable. The variance is mainly contributed by the measurement error, a softer spring from the fabrication process and the position error between actuation coil and magnet. Meanwhile, because of the weight of the magnet is around 5 mg, the displacement in Y direction without applying current is around 8 μm caused by the gravity of suspending magnet. Therefore, the displacement in Y direction was increased from around 8 μm to 25 μm as shown in Fig. 16b, d and f. The magnet was pulled by the PCB when actuated by DC current and the value of the displacement in Y direction was negative regardless the displacement in X direction.

## 4. Conclusion

The rare earth magnetic powder Sm-Fe-N was utilized to fabricate micro magnets. By conducting the alignment of the easy axis process, the remanence of the micro magnet was significantly enhanced. The properties of the magnets with different weight loading percentage of magnetic powder were investigated by utilizing a VSM. As the results show that, with the increase loading of magnetic powder, both remanence and energy product increased. The coercivity remained almost the same when the wax was sufficient to bond the powder. However, both remanence and coercivity decreased significantly when the wax was scare to bond the magnetic powder. In the best condition, the remanence reaches 0.9 T and the energy product reaches 70 kJ/m$^3$. This is the best performance ever reported for micro magnets in Si except for thin films. Nevertheless, still improvement could be made to increase the properties of the magnet by increasing the density of the magnet. In our samples, the magnetic powder was filled into the cavities by manually, which means the density was not so large. High pressure could be helpful in fabricating a magnet with much higher density.

Magnetic simulation was performed to study the Lorentz force generated by the coupling between the current and the magnetic field. The displacements in both X and Y direction are predicted. The actuators with various magnetic powder weight loading percentage were fabricated. By the application of DC current, the actuator could reach 180 μm in-plane displacement and 17 μm out-of-plane displacement. The measured results are identical with the simulation which proved that the prediction of the displacement was reasonable. The results of the actuation revealed that the fabrication of the magnet made from the rare earth magnetic powder Sm-Fe-N was successful and this powder is promising in MEMS devices.

## 5. Reference


[1] Y. S. Kim, N. G. Dagalakis, and S. K. Gupta, 2014 Design of MEMS based three-axis motion stage by incorporating a nested structure *J. Micromech. Microeng.* 24 075009

[2] M. U. Khan, N. Bencheikh, C. Prelle, F. Lamarque, T. Beutel and S. Buttgenbach 2012 A Long Stroke Electromagnetic XY Positioning Stage for Micro Applications *IEEE/ASME Trans. Mechatronics* 17 866-875

[3] J. S. Han, J. S. Ko, and J. G. Korvink 2004 Structural optimization of a large-displacement electromagnetic Lorentz force microactuator for optical switching applications *J. Micromech. Microeng.*14 1585–1596

[4] R. Chauhan and M. Pandey 2016 Flexures for large stroke electrostatic comb-drive actuators *Int. Conf. Microelectron. Comput. Commun. MicroCom.* 1 1–6

[5] D. J. Bell, T. J. Lu, N. A. Fleck, and S. M. Spearing 2005 MEMS actuators and sensors: Observations on their performance and selection for purpose *J. Micromech. Microeng.* 15 S153-64

[6] R. Xiao, S. Shao, M. Xu, and Z. Jing 2019 Design and Analysis of a Novel Piezo-Actuated XYθz Micropositioning Mechanism with Large Travel and Kinematic Decoupling *Adv. Mater. Sci. Eng.* 2019 1-15

[7] Y. S. Kim, H. Shi, N. G. Dagalakis, and S. K. Gupta 2016 Design of a MEMS-based motion stage based on a lever mechanism for generating large displacements and forces *J. Micromech. Microeng.* 26 95008

[8] A. Pimpin, I. Charoenbunyarit, and W. Srituravanich 2017 Material and performance characterization of Z-shaped nickel electrothermal micro-actuators *Sens. Actuators, A.* 253 49–58

[9] Y. Fujimura, T. Tsukamoto, and S. Tanaka 2017 Piezoelectric Moonie-type resonant microactuator *IEEJ Trans. Sensors Micromachines* 137 95–100

[10] Y. Fujimura, T. Tsukamoto, and S. Tanaka 2018 2-axis resonant microstage using single piezoelectric moonie-type Microactuator *IEEJ Trans. Sensors Micromachines* 138 516–522

[11] S. Yoshida, N. Wang, M. Kumano, Y. Kawai, S. Tanaka, and M. Esashi 2013 Fabrication and characterization of laterally-driven piezoelectric bimorph MEMS actuator with sol-gel-based high-aspect-ratio PZT structure *J. Micromech. Microeng.* 23 065014

[12] D. Zhang, C. Chang, T. Ono, and M. Esashi 2003 A piezodriven XY-microstage for multiprobe nanorecording *Sens. Actuators, A.* 108 230–233

[13] J. C. Chiou and Y. J. Lin 2005 A novel large displacement electrostatic actuator: Pre-stress comb-drive actuator *J. Micromech. Microeng.* 15 1641–1648

[14] M. Olfatnia, S. Sood, J. J. Gorman, and S. Awtar 2013 Large stroke electrostatic comb-drive actuators enabled by a novel flexure mechanism *J. Microelectromech. Syst.* 22 483–494

[15] M. Olfatnia, L. Cui, P. Chopra, and S. Awtar 2013 Large range dual-axis micro-stage driven by electrostatic comb-drive actuators *J. Micromech. Microeng.* 23 105008

[16] G. Zhou and P. Dowd 2003 Tilted folded-beam suspension for extending the stable travel range of comb-drive actuators *J. Micromech. Microeng.* 13 178–183

[17] J. D. Grade, H. Jerman, and T. W. Kenny 2003 Design of large deflection electrostatic actuators *J. Microelectromech. Syst.* 12 335–343

[18] C. Chen and C. Lee 2004 Design and modeling for comb drive actuator with enlarged static displacement *Sens. Actuators, A.* 115 530–539

[19] A. D. Yalcinkaya, H. Urey, D. Brown, T. Montague, and R. Sprague 2006 Two-axis electromagnetic microscanner for high resolution displays *J. Microelectromech. Syst.* 15 786–794

[20] H. Urey, S. Holmstrom, U. Baran, K. Aksit, M. K. Hedili, and O. Eides 2013 MEMS scanners and emerging 3D and interactive Augmented Reality display applications *17th Int. Conf. Solid-State Sensors, Actuat. Microsys., Transducers Eurosensors* 2013 2485–2488

[21] M. Peng, X. Zhu, B. Jiang, T. Zhou, and Y. Su 2019 Air damping characteristics of a 2D MEMS electromagnetically driven micro-mirror *Microsyst. Technol.* 25 2675–2682

[22] H. Miyajima 2004 Development of a MEMS electromagnetic optical scanner for a commercial laser scanning microscope *J. Microlithogr. Microfabr. Microsys.* 3 348–357

[23] Kim, J. et al. 2015 Electromagnetically actuated 2-axis scanning micromirror with large aperture and tilting angle for lidar applications *18th Int. Conf. Solid-State Sensors, Actuat. Microsys., Transducers* 2015 839-842

[24] B. Jiang, M. Peng, Y. Liu, T. Zhou, and Y. Su 2019 The fabrication of 2D micromirror with large electromagnetic driving forces *Sens. Actuators, A*. 286 163–168

[25] C. H. Ji, M. Choi, S. C. Kim, K. C. Song, J. U. Bu, and H. J. Nam 2007 Electromagnetic two-dimensional scanner using radial magnetic field *J. Microelectromech. Syst.* 16 989–996

[26] Q. Cao, Y. Tan, R. Dong, and W. Shen 2020 A Modeling Method of Electromagnetic Micromirror in Random Noisy Environment *IEEE Trans. Syst. Man, Cybern. Syst.* 50 2578–2587

[27] N. Asada, M. Takeuchi, V. Vaganov, N. Belov, S. In'T Hout, and I. Sluchak 2000 Silicon micro-optical scanner *Sens. Actuators, A.* 83 284–290

[28] S. D. Tisnés, Z. Shi, L. Petit, C. Prelle and F. Lamarque 2019 Characterization of a micro-fabricated digital actuator array as a micro-factory conveyor device *IEEE/ASME Int. Conf. Advanced Intelligent Mechatronics (AIM)* 382-387

[29] C. L. Hsieh, C. S. Liu, and C. C. Cheng 2020 Design of a 5 degree of freedom–voice coil motor actuator for smartphone camera modules *Sens. Actuators, A*. 309 112014

[30] P. Pournazari, R. Nagamune, and M. Chiao 2014 A concept of a magnetically-actuated optical image stabilizer for mobile applications *IEEE Trans. Consum. Electron.* 60 10–17

[31] M. G. Song et al. 2010 Development of small sized actuator with compliant mechanism for optical image stabilization *IEEE Trans. Magn.* 46 2369–2372

[32] M. G. Song, N. C. Park, K. S. Park, and Y. P. Park, 2011 Improvement of an asymmetric actuator for optical image stabilization *Microsyst. Technol.* 17 1231–1241

[33] P. Zhao, R. Nagamune, and M. Chiao 2018 Multiple parameter-dependent robust control of miniaturized optical image stabilizers *Contr. Eng. Pract.* 76 1–11

[34] K. Tao et al. 2017 Micro-patterning of resin-bonded NdFeB magnet for a fully integrated electromagnetic actuator *Solid-State. Electron.* 138 66–72

[35] D. Han, T. Shinshi, N. Azuma, and S. Kadota 2019 An in-plane, large-stroke, multipole electromagnetic microactuator realized by guideways stacking mechanism *Sens. Actuators, A.* 298 111563

[36] Y. Wang, B. Y. Jimenez and D. P. Arnold 2020 100-µm-Thick High-Energy-Density Electroplated CoPt Permanent Magnets *IEEE 33rd Int. Conf. Micro Electro Mech. Sys. (MEMS)* 558-561

[37] R. Molian and P. M. Ã 2009 Pulsed laser deposition and annealing of Dy–Fe–B thin films on melt-spun Nd–Fe –B ribbons for improved magnetic performance *J. Magn. Magn. Mater.* 321 241–246

[38] M. Nakano et al. 2015 Nd–Fe–B Film Magnets With Thickness Above 100 µm Deposited on Si Substrates *IEEE Trans. Magn.* 51 1-4

[39] O. D. Oniku, B. Qi, and D. P. Arnold 2016 Journal of Magnetism and Magnetic Materials Electroplated thick- fi lm cobalt platinum permanent magnets *J. Magn. Magn. Mater.* 416 417–428

[40] G. V. Ramana, P. Saravanan, S. V Kamat, and Y. Aparna 2012 Applied Surface Science Optimization of sputtering parameters for Sm Co thin films using design of experiments *Appl. Surf. Sci.* 261 110–117

[41] A. Walther, C. Marcoux, B. Desloges, R. Grechishkin, D. 2008 Micro-patterning of NdFeB and SmCo magnetfilms for integration into micro- electro-mechanical-system *J. Magn. Magn, Mater.* 321 590-594

[42] Y. Wang, R. Bowrothu, Y. Yoon, and D. P. Arnold 2019 Patterning of thick electroplated CoPt magnets using SU-8 micromoulds *Micro & Nano Lett.* 14 1393–1396

[43] O. D. Oniku, B. J. Bowers, S. B. Shetye, N. Wang, and D. P. Arnold 2013 Permanent magnet microstructures using dry-pressed magnetic powders *J. Micromech. Microeng.* 23 2013

[44] H. Li, T. J. Flynn, J. C. Nation, J. Kershaw, L. Scott Stephens, and C. A. Trinkle 2013 Photopatternable NdFeB polymer micromagnets for microfluidics and microrobotics applications *J. Micromech. Microeng.* 23 2013

[45] B. J. Bowers, J. S. Agashe, and D. P. Arnold 2007 A method to form bonded micromagnets embedded in silicon *4th Int. Conf. Solid-State Sens., Actuat. Microsys., Transducers Eurosensors* 1585–1588

[46] H. J. Cho and C. H. Ahn 2003 Microscale resin-bonded permanent magnets for magnetic micro-electro-mechanical systems applications *J. Appl. Phys.* 93 8674–8676

[47] N. G. Akdogan and O. Akdogan 2019 Synthesis of Nd-Fe-B / Fe hybrid micro- magnets *64th Int. Conf. Magn. Magn. Mater.* 9 125139

[48] T. Lisec et al. 2019 Integrated High Power Micro Magnets for MEMS Sensors and Actuators 20th Int. Conf. Solid-State Sens., Actuat. Microsys. Transducers Eurosensors 1768-1771

[49] W. Makishi, Y. Kawai and M. Esashi 2009 Magnetic torque driving 2D micro scanner with a non-resonant large scan angle

*'09 Int. Conf. Solid-State Sens., Actuat. Microsys. Transducers* 904-907

[50] A. You, M. A. Y. Be, and I. In 2014 Demagnetizing factors for rectangular ferromagnetic prisms *J. Appl. Phys.* 3432 4–7

[51] N. Wang, B. J. Bowers, and D. P. Arnold 2008 Wax-bonded NdFeB micromagnets for microelectromechanical systems applications *J. Appl. Phys.* 103 2008